Supporting Information for "Flexure of the lithosphere beneath the north polar cap of Mars, with implication for ice compositions and heat flow"

A. Broquet[1]*, M. A. Wieczorek[1], W. Fa[2,3]

[1]Université Côte d'Azur, Observatoire de la Côte d'Azur, CNRS, Laboratoire Lagrange, Nice, France.

[2]Institute of Remote Sensing and Geographical Information System, School of Earth and Space Sciences, Peking University, Beijing, China.

[3]State Key Laboratory of Lunar and Planetary Sciences, Macau University of Science and Technology, Macau, China.

Contents of this file

1. Text S1 to S5
2. Figures S1 to S6

Introduction. In this supporting information, we compare SHARAD and MARSIS data, discuss the uncertainties in the inversion, show an additional inversion using SHARAD data, and detail some of the processing steps to constrain the composition of the north polar cap. We conclude showing a simple viscoelastic model in order to estimate whether the north polar cap is at elastic equilibrium.

Text S1: MARSIS versus SHARAD

We investigated SHARAD data to ensure that they were in good agreement with our thickness estimates using MARSIS, as SHARAD generally has a better range resolution than MARSIS. On the left of Figure S2, we show as filled circles, the differences between the apparent thickness of the north polar cap derived using MARSIS and SHARAD. Points filled in white represent locations where we did not find a subsurface echo in SHARAD radargrams. We observe a bimodal distribution, where the SHARAD thickness estimates are consistent with MARSIS in places where the basal unit is not predicted to be present below the north polar layered deposits, and largely different where the basal unit is present (for a map of the extent of the basal unit, see Selvans et al., 2010). We interpret this as a limitation of the resolution of SHARAD, which is not always able to penetrate through the sand-rich basal unit (see also Nunes & Phillips, 2006). Where there is no basal unit, the average apparent difference between MARSIS and SHARAD is 45 meters and the standard deviation is 131 meters, which is close to the 150 meters range resolution of MARSIS in free-space.

On the right side, we show examples of radar echo strengths as a function of the apparent depth at two locations, one where the basal unit is present below the north polar layered deposits (top) and one in Gemina Lingula, where the basal unit is not present (bottom). The two locations are displayed as triangles on the left image. In the upper image, we observe that the first associated with reflections from the surface (fixed at a depth of 0 km) and the top of the basal unit (depth 2.1 km) correlate well between MARSIS and SHARAD. A slight offset of about 150 meters between the peak associated with the top

of the basal unit is noticed, which is likely due to the difference in range resolution of the two instruments. However, the SHARAD radargram does not show evidence for a third peak that is associated with the base of the polar cap as seen by MARSIS. In the bottom plot, we observe that the echoes from the surface and base of the polar cap of SHARAD and MARSIS correlated well, through we again do have slight offsets that are comparable to the range resolutions of the instruments. An intermediate peak between these two reflectors is also seen and is likely due to layering in the polar cap (the basal unit is not believed to be present in this region, Selvans et al., 2010). In this frame, we note that there is a deeper peak at an apparent depth of 3.3 km (corresponding to about 300 meters below the base of the polar cap) for both SHARAD and MARSIS, but this reflector showed no continuity in adjacent frames and was hence interpreted as a spurious subcrustal reflector.

Text S2: Uncertainties in the inversion

In order to place bounds on the range of acceptable parameters in our inversions, it is necessary to define a maximum allowable rms misfit between our model and the observations. Several sources of uncertainty will contribute to this value.

First, the inherent range resolution of a radar in free-space is approximately half its wavelength. For MARSIS, which has an instantaneous frequency of 1 MHz (Picardi et al., 2005), the uncertainty in free-space is 150 m and is 86.5 m in water ice ($\varepsilon = 3$).

A second source of uncertainty comes from surface roughness along an interface. The roughness of the surface can cause multiple reflections and scattering of the radio wave that makes the subsurface echo appear as a wide peak. Picking the subsurface reflector

location (in unit of time) in the radargrams will then be associated with an uncertainty that is about the pulse width of the echo. The pulse width of the peaks associated with the surface and subsurface echoes for MARSIS are generally about 3 pixels or 321 m in free-space and 185 m in water ice (see Figure S2). We verified that this value, to be used as an uncertainty, is reasonable by computing the surface roughness of MOLA elevation data at the scale of the Fresnel zone. The Fresnel zone gives the typical length at which a radio wave interacts with the surrounding media and can be estimated as $2 \times \sqrt{D\lambda/2}$, where D is the distance of the spacecraft from the surface and λ its wavelength. For MARSIS, D over the north pole is about 900 km, which gives a Fresnel zone diameter of 23 km. The surface roughness of the north polar cap within 23 km diameter circles was found to vary from few meters where the polar cap is smoothest to 250 m near the edge of the polar cap and troughs, which is consistent with the estimation using the pulse width.

A third source of uncertainty comes from the shape of the pre-loading surface. To determine the uncertainty in the pre-loading surface, we varied the limits of the annulus of topographic data exterior to the polar cap used in the interpolation. We obtained that the pre-loading surfaces differed by no more than 170 m on average beneath the polar cap.

Assuming these three sources of error are independent, the rms uncertainty in the inversion for MARSIS is 266 m. For SHARAD, the uncertainties are: 8.6 m for the range resolution in water ice, 40 m uncertainty from the pulse width of the subsurface echoes (that is in good agreement with the surface roughness at the 3 km scale of the Fresnel zone), and the 170 m uncertainty from the basal interpolation. This gives an rms error of

175 m. These uncertainties are generally higher than those found in Selvans et al. (2010) (200 m for MARSIS) or Phillips et al. (2008) (100 m for SHARAD), because of the large uncertainty from the estimation of the pre-loading surface.

Text S3: Constraints on the composition of the north polar cap

CO_2 ice has a smaller thermal conductivity than water ice, which would give rise to higher internal temperatures within the polar can that could lead to basal melting. Basal melting, however, has not been observed from radar studies at the north pole. We therefore added the constraint that no basal melting should occur at present-day where radar observations are present. We used a Maxwell-Garnett mixing law to compute the thermal conductivity of mixtures (Sihvola, 2000) and solved for the temperature gradient using Fourier's law of heat conduction. In the mixing law, it was assumed that the matrix was the component with the largest volumetric abundance and that the two others were considered as randomly spaced spherical inclusions. From the temperature profiles, we checked whether the melting point of CO_2 ($\sim$ 216 K) was exceeded (H_2O has a warmer melting point, $\sim$ 273 K). Heat flows from 20 to 35 mW m^{-2} were employed (Plesa et al., 2018), a surface temperature of 155 K was assumed, and thermal conductivities of 4, 0.75, 0.75, and 3 W m^{-1} K^{-1} were used for H_2O, CO_2, clathrates and dust (Wieczorek, 2008).

A Maxwell-Garnett mixing law for a three-phase mixture was used when computing the dielectric constant of mixtures. For water ice, we used a dielectric constant of 3 (see experimental data by Pettinelli et al., 2003; Phillips et al., 2008). A real dielectric constant of 3 is the value used by the MARSIS team for water ice (Selvans et al., 2010), whereas a value of 3.15 is usually used by the SHARAD team (Grima et al., 2009). Increasing the

dielectric constant of water ice would increase the amount of both CO_2 and clathrate ices in the polar cap that is predicted by our model. We also set a dielectric constant of 2.2, 2.85 and 6, respectively for CO_2 and clathrate ices, and dust (Wieczorek, 2008; Nunes & Phillips, 2006).

With two constraints (density and dielectric constant), it would be possible to invert only for the abundances of mixtures of two components uniquely. Here, we consider 3 component mixtures, and plot the possible solutions in a ternary diagram. As we consider 4 possible components (CO_2, water ice, dust, and clathrates), we show 3 separate ternary diagrams were one of the four components was assumed to be absent. The range of allowable density and dielectric constant vary as a function of the elastic thickness, and therefore, in this figure, we show two end-member cases for an elastic thickness of 330 (top) and 400 (bottom) km. We observe that in all cases, the north polar cap has a minimum of 24% to 42% water ice if we ignore models that generate basal melting for heat flows of 20 to 25 mW m^{-2}. The plots in the left column are described in the main text. If there is no CO_2 inside the north polar cap, but instead clathrate ices, then there must be a minimum of 77% to 58% of clathrates within the polar cap for heat flows of 20 to 25 mW m^{-2}.

Text S4: Conversion of elastic thickness to heat flow

The method to convert an elastic thickness into a heat flow was pioneered by McNutt (1984) (see also Broquet & Wieczorek, 2019). This involves setting the bending moment of a fictive elastic plate equal to that of the bending stresses in a more realistic rheology that considers maximum yielding stresses from fracturing and viscous flow. The bending

stresses of the elastic plate can be found analytically if one knows the elastic parameters of the plate and the curvature. For an elastic thickness of 330 km and surface density of 1100 kg m^{-3}, the maximum curvature beneath the north polar cap, defined as the second spatial derivative of the deflection, is 7.4 $\times 10^{-10}$ m^{-1}. The bending stresses of the realistic plate will depend upon its rheology and temperature. For this, we used a wet diabase rheology for the crust, and dry olivine for the mantle (Plesa et al., 2018), a strain rate of 10^{-14} s^{-1} and a low bounding stress of 10 MPa (Phillips et al., 2008), and a thermal conductivity of respectively 3 and 4 W m^{-1} K^{-1} for the crust and mantle.

When computing the temperature profile, we considered the effects of radioactive elements within both the crust and mantle. For the crust, we used the derived surface heat production of 4.9 $\times 10^{-11}$ W kg^{-1} (Hahn et al., 2011) and following Plesa et al. (2018) we set the mantle heat production to 10% of that value. We then simply varied the heat flow at the base of the lithosphere until both bending stresses converged. For an elastic thickness of 330 km, the best-fitting surface heat flow we obtained is 16 mW m^{-2}, which is in good agreement with thermal evolution models from Plesa et al. (2018). Ignoring the presence of radioactive elements in the crust gives a slightly smaller heat flow of 14 mW m^{-2}, where the difference is simply the heat production in the crust (2 mW m^{-2}). Because the crust is thin in the north polar region, the heat flow contribution from the crust is generally low (see also Plesa et al., 2016). If the elastic thickness is set to 450 km, then the heat flow is reduced to 11 mW m^{-2}.

Text S5: Influence and timescale of viscous relaxation

In our deflection model, the lithosphere is purely elastic and the mantle is treated as an inviscid fluid such that shell deformations are instantaneous and not subject to viscous relaxation. The latter is only a valid assumption if the time that has elapsed since the polar cap formed is larger than the time required for viscous adjustments. But, if the age of the polar cap is comparable to the viscous relaxation time, it is possible that the north polar load is in a transient state where the lithosphere is still adjusting viscously. In that case, the present-day topography and flexure reflect not only the current cap geometry but also the time-integrated history of the polar cap load. The loading history of the north polar deposits is potentially complex with cycles of loading and unloading of the lithosphere. In periods of low obliquity, perennial ice forms and in high obliquity periods, ice sublimates and the polar cap decreases in size (Kieffer & Zent, 1992). These periods alternate quickly on million years timescale, as the obliquity of Mars is thought to be mostly chaotic (Jakosky et al., 1995; Laskar et al., 2004).

Crater counting and thickness evolution estimates from Global Climate Models of the north polar deposits agree generally with the idea that the icy deposits are about 1 million years old (Levrard et al., 2007; Herkenhoff & Plaut, 2000). Using the ALMA code of Spada (2008) we computed load Love numbers for a simple four layer Martian interior model based on Phillips et al. (2008). The h' load Love number is a degree (l) dependent linear transfer function that links the load potential (V) to the radial displacement, in our case the deflection (W), as

$$W_{l,m} = \frac{V_{l,m}}{g_0}\, h'_l, \tag{1}$$

where g_0 is the gravitational acceleration at the surface and m is the angular order.

In Figure S6, we show the evolution of the degree-8 load Love number, which corresponds to the scale of the cap, as a function of time. The time before equilibrium is achieved (i.e., the long term asymptote) is found to vary from 10^4 to 10^8 years for mantle viscosities of 10^{19} and 10^{23} Pa s. We note the time to achieve equilibrium depends upon the harmonic degree and would be about 2 times lower for the degree-20 load Love number. The viscosity of the Martian mantle today is thought to range from 10^{20} to 10^{22} Pa s (Plesa et al., 2018), and this limits the time for equilibrium to a range from 10^5 to 10^7 year. This timescale does not allow to rule out the possibility that the polar cap is in a transient state that has not yet achieved equilibrium. As an example, if the north polar cap is 1 million years old and the viscosity of the mantle is 10^{22} Pa s, then it is possible that we are currently observing only about 50% of the final degree-8 deflection below the cap. Assuming that we are observing 50% of the total (i.e. for all degrees) and final deflection below the cap, then the elastic thickness at equilibrium could be as low as 150 km. However, if the cap is 1 million years old and the viscosity of the mantle is 10^{21} Pa s, then our viscoelastic model predicts that the we currently observing the final deflection.

References

Broquet, A., & Wieczorek, M. A. (2019). The gravitational signature of Martian volcanoes. *Journal of Geophysical Research: Planets*, *124*(8), 2054–2086. doi: 10.1029/2019JE005959

Grima, C., Kofman, W., Mouginot, J., Phillips, R. J., Hérique, A., Biccari, D., ... Cutigni, M. (2009). North polar deposits of Mars: Extreme purity of the water ice. *Geophysical Research Letters*, *36*(L03203). doi: https://doi.org/10.1029/

2008GL036326

Hahn, B. C., McLennan, S. M., & Klein, E. C. (2011). Martian surface heat production and crustal heat flow from Mars Odyssey Gamma-Ray spectrometry. *Geophysical Research Letters*, *38*(14). doi: https://doi.org/10.1029/2011GL047435

Herkenhoff, K. E., & Plaut, J. J. (2000). Surface Ages and Resurfacing Rates of the Polar Layered Deposits on Mars. *Icarus*, *144*(2), 243-253. doi: https://doi.org/10.1006/icar.1999.6287

Jakosky, B. M., Henderson, B. G., & Mellon, M. T. (1995). Chaotic obliquity and the nature of the martian climate. *Journal of Geophysical Research: Planets*, *100*(E1), 1579-1584. doi: https://doi.org/10.1029/94JE02801

Kieffer, H. H., & Zent, A. P. (1992). Quasi-periodic climate change on Mars. In H. H. Kieffer, B. M. Jakosky, C. W. Snyder, & M. S. Matthews (Eds.), *Mars* (p. 1180-1218). Univ. of Arizona Press, Tuscon.

Laskar, J., Correia, A., Gastineau, M., Joutel, F., Levrard, B., & Robutel, P. (2004). Long term evolution and chaotic diffusion of the insolation quantities of mars. *Icarus*, *170*(2), 343 - 364. doi: https://doi.org/10.1016/j.icarus.2004.04.005

Levrard, B., Forget, F., Montmessin, F., & Laskar, J. (2007). Recent formation and evolution of northern martian polar layered deposits as inferred from a global climate model. *Journal of Geophysical Research: Planets*, *112*(E6). doi: https://doi.org/10.1016/10.1029/2006JE002772

McNutt, M. K. (1984). Lithospheric flexure and thermal anomalies. *Journal of Geophysical Research: Solid Earth*, *89*(B13), 180–194. doi: https://doi.org/10.1029/

JB089iB13p11180

Nunes, D. C., & Phillips, R. J. (2006). Radar subsurface mapping of the polar layered deposits on mars. *Journal of Geophysical Research: Planets*, *111*(E6). doi: https://doi.org/10.1029/2005JE002609

Pettinelli, E., Vannaroni, G., Cereti, A., Paolucci, F., Della Monica, G., Storini, M., & Bella, F. (2003). Frequency and time domain permittivity measurements on solid co2 and solid co2 soil mixtures as martian soil simulants. *Journal of Geophysical Research: Planets*, *108*(E4). doi: https://doi.org/10.1029/2002JE001869

Phillips, R. J., Zuber, M. T., Smrekar, S. E., Mellon, M. T., Head, J. W., Tanaka, K. L., ... Marinangeli, L. (2008). Mars North Polar Deposits: Stratigraphy, Age, and Geodynamical Response. *Science*, *320*(5880), 1182–1185. doi: https://doi.org/10.1126/science.1157546

Picardi, G., Plaut, J. J., Biccari, D., Bombaci, O., Calabrese, D., Cartacci, M., ... Zampolini, E. (2005). Radar soundings of the subsurface of Mars. *Science*, *310*(5756), 1925–1928. doi: https://doi.org/10.1126/science.1122165

Plesa, A.-C., Grott, M., Tosi, N., Breuer, D., Spohn, T., & Wieczorek, M. A. (2016). How large are present-day heat flux variations across the surface of Mars? *Journal of Geophysical Research: Planets*, *121*(12), 2386–2403. doi: https://doi.org/10.1002/2016JE005126

Plesa, A.-C., Padovan, S., Tosi, N., Breuer, D., Grott, M., Wieczorek, M. A., ... Banerdt, W. B. (2018). The thermal state and interior structure of mars. *Geophysical Research Letters*, *45*(22), 12,198-12,209. doi: https://doi.org/10.1029/2018GL080728

Selvans, M. M., Plaut, J. J., Aharonson, O., & Safaeinili, A. (2010). Internal structure of Planum Boreum, from Mars advanced radar for subsurface and ionospheric sounding data. *Journal of Geophysical Research: Planets*, *115*(E9). doi: https://doi.org/10.1029/2009JE003537

Sihvola, A. (2000, Oct 01). Mixing rules with complex dielectric coefficients. *Subsurface Sensing Technologies and Applications*, *1*(4), 393–415. doi: https://doi.org/10.1023/A:1026511515005

Smith, & Wessel. (1990). Gridding with continuous curvature splines in tension. *Geophysics*, *55*(3), 293-305. doi: https://doi.org/10.1190/1.1442837

Spada, G. (2008). Alma, a fortran program for computing the viscoelastic love numbers of a spherically symmetric planet. *Computers & Geosciences*, *34*(6), 667 - 687. doi: https://doi.org/10.1016/j.cageo.2007.12.001

Wieczorek, M. A. (2008). Constraints on the composition of the Martian south polar cap from gravity and topography. *Icarus*, *196*, 506–517. doi: https://doi.org/10.1016/j.Icarus.2007.10.026

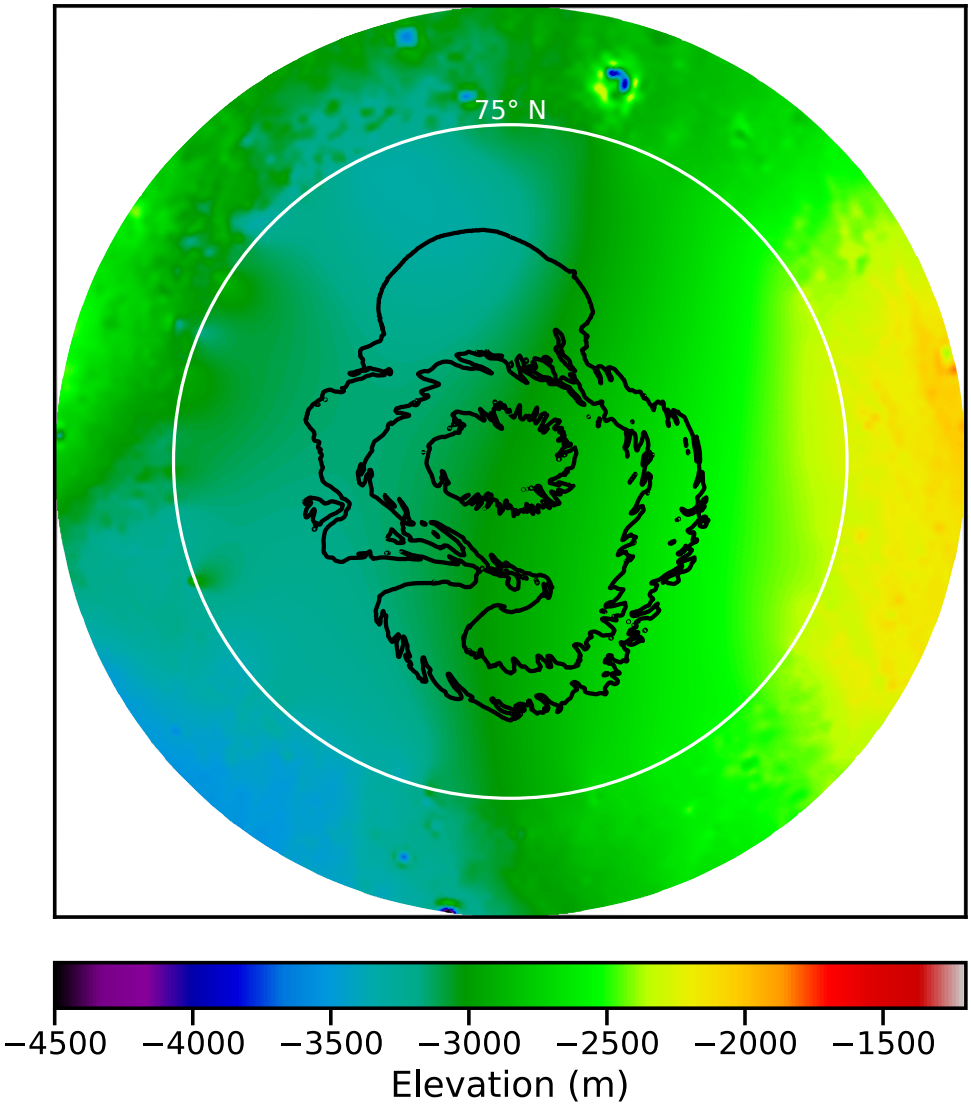

Figure S1. The pre-loading surface poleward 70°N, h_0, estimated using an annulus of MOLA elevation data exterior to the north polar cap between 70°N to 75°N and interpolated poleward using the minimum curvature method of Smith and Wessel (1990). For geologic purposes, elevation contours of the polar cap are shown in black.

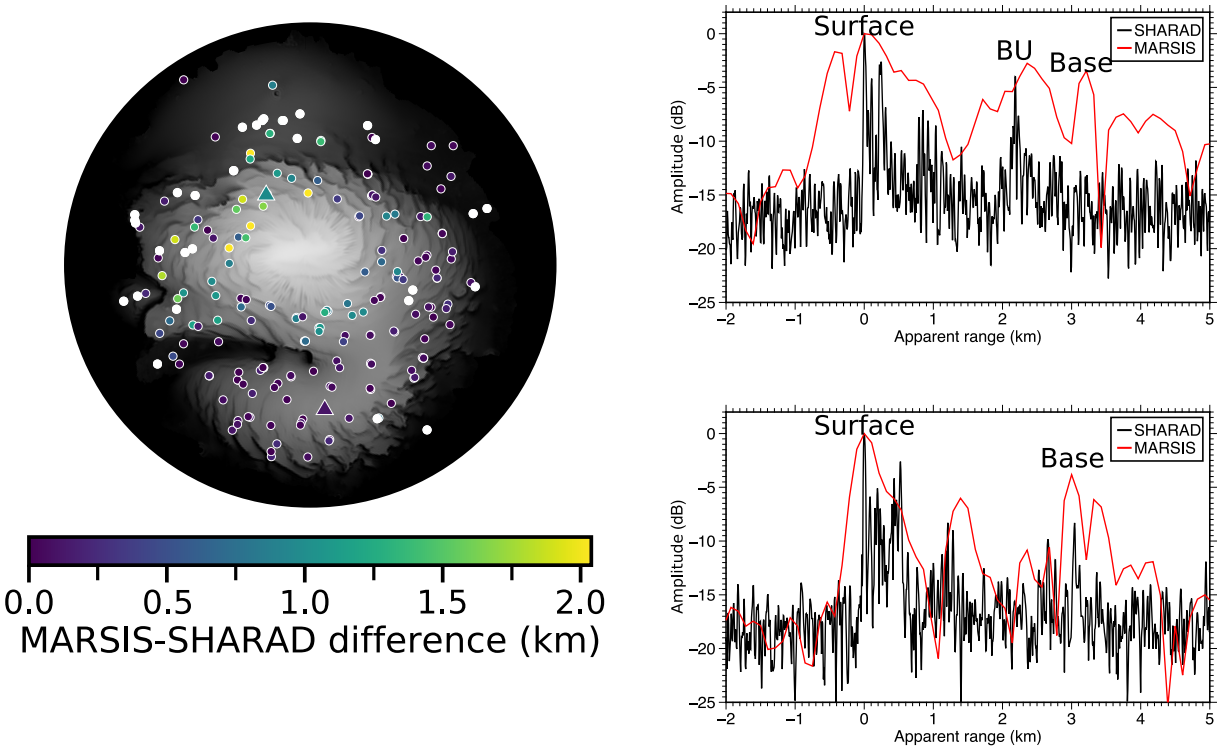

Figure S2. (left) Difference between the apparent thickness of the north polar cap as seen by MARSIS and SHARAD at 213 locals. Circles filled in white show locations where we did not detect a subsurface echo in the SHARAD radargrams. A bimodal distribution is observed, and is due to the inability of SHARAD to see beneath the basal unit when it is present. (right) Echo strength versus the converted apparent range of SHARAD and MARSIS at the location of the 2 triangles (top, latitude 86.26, longitude 212.42, MARSIS orbit 9576, SHARAD orbit 878503 bottom, latitude 81.97, longitude 7.12, MARSIS orbit 3698, SHARAD orbit 3656701) in the left figure. Echoes associated with the reflection from the surface is seen to correlate well between MARSIS and SHARAD. The base of the polar cap is not detected by SHARAD in the upper right image, which is due to the presence of the basal unit.

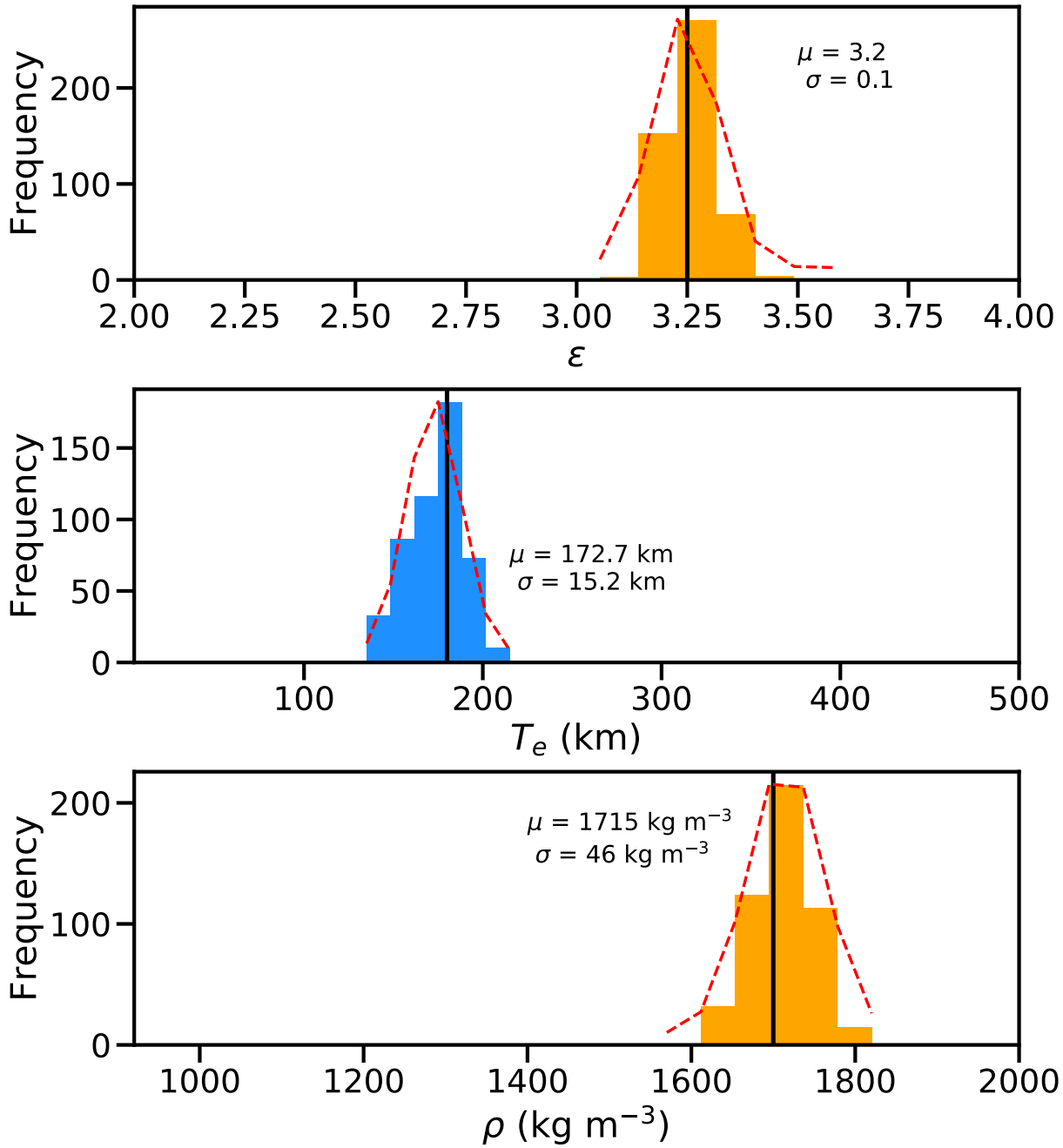

Figure S3. Histograms for the maximum accepted dielectric constant, minimum accepted elastic thickness and maximum accepted ice density following 500 inversions where 50% of the MARSIS data points were randomly selected. The average, μ, and standard deviation, σ, is provided for each of the distributions. The black vertical lines show the inversion results using all MARSIS data points.

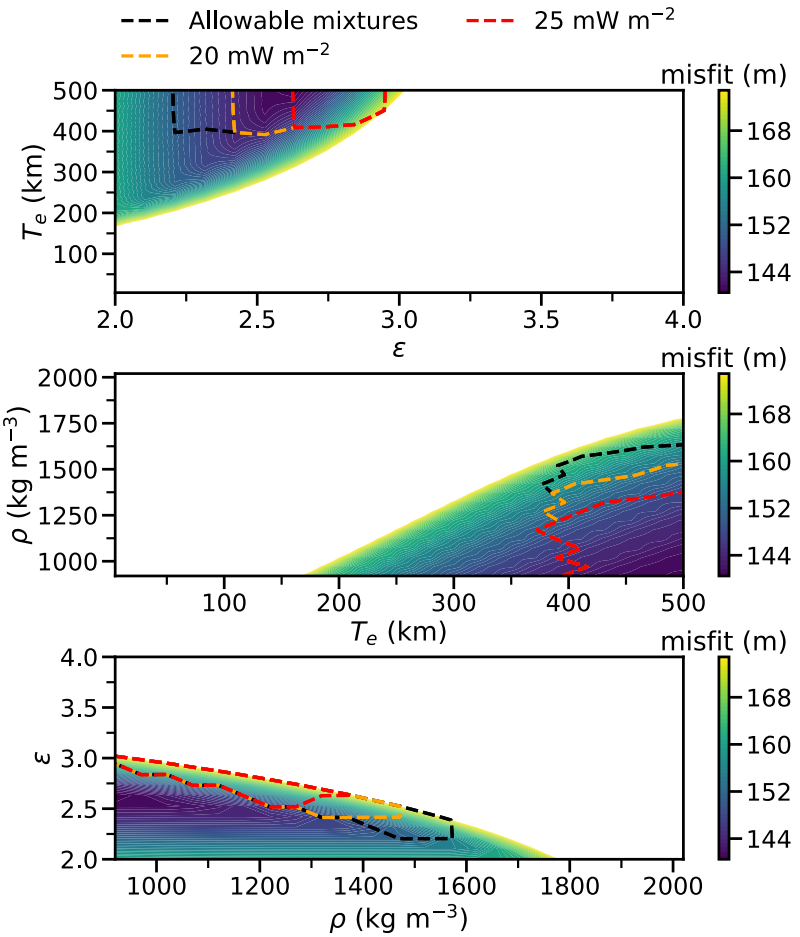

Figure S4. Minimum rms misfit as a function of the dielectric constant (ε), elastic thickness (T_e), and bulk density of the polar cap (ρ) using SHARAD data at 78 locations. The color corresponds to the rms misfit that is cut off at 175 m. The black line delimits possible mixtures, and the red and orange lines delimit those same mixtures that do not produce basal melting for heat flows of 20 and 25 mW m^{-2}. Assuming that the heat flow at the north pole is 20 mW m^{-2}, the real dielectric constant is found to range from 2.4 to 3.0, the elastic thickness is at least 370 km, and the density ranges from 920 to 1570 kg m^{-3}.

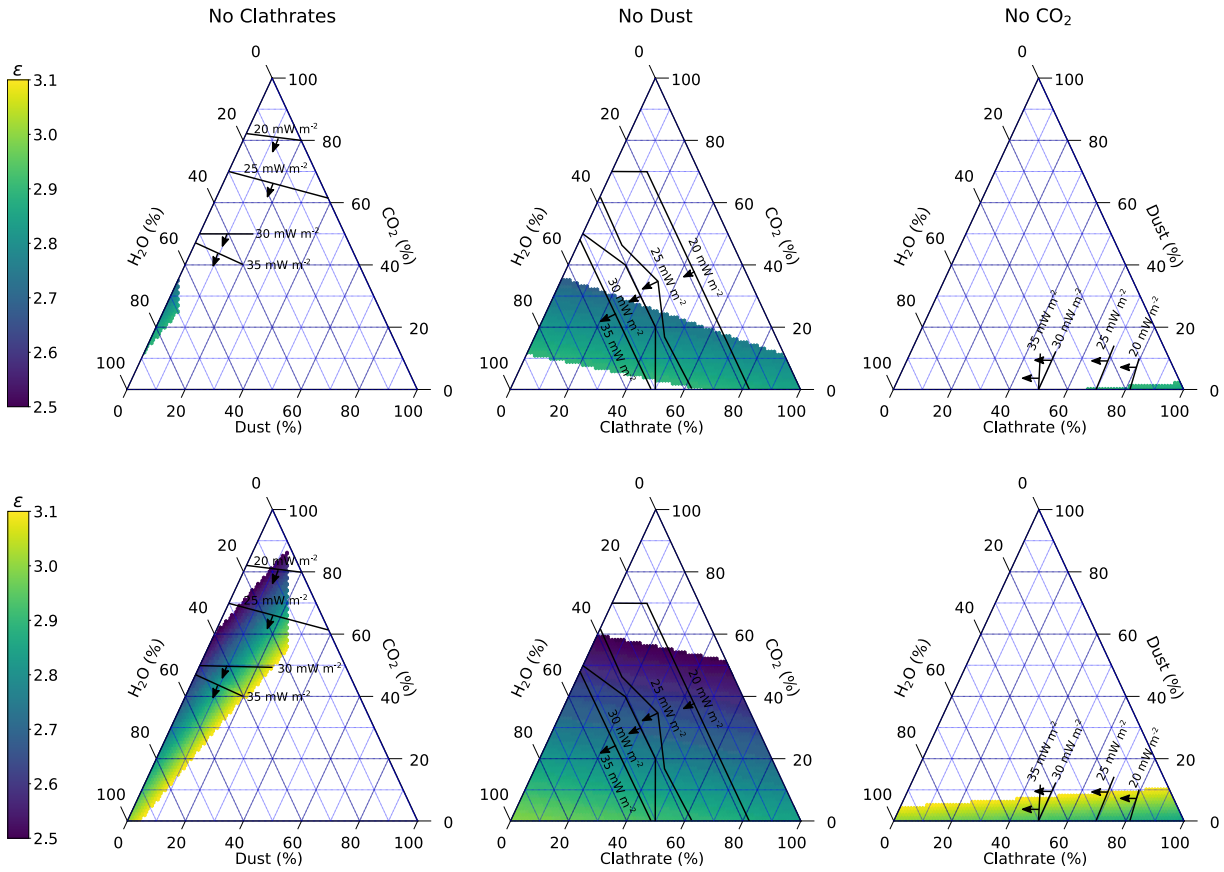

Figure S5. Ternary plots for allowable volumetric mixtures of ices and dust, where one of the four components is absent. Results are shown for two elastic thicknesses, $T_e = 330$ and 400 km (top and bottom), and the color for each allowable mixture corresponds to the real dielectric constant. The black lines limit the regions above witch basal melting would occur as a function of various heat flows from 20 to 35 mW m^{-2}. Acceptable solutions are in the direction given by the black arrows.

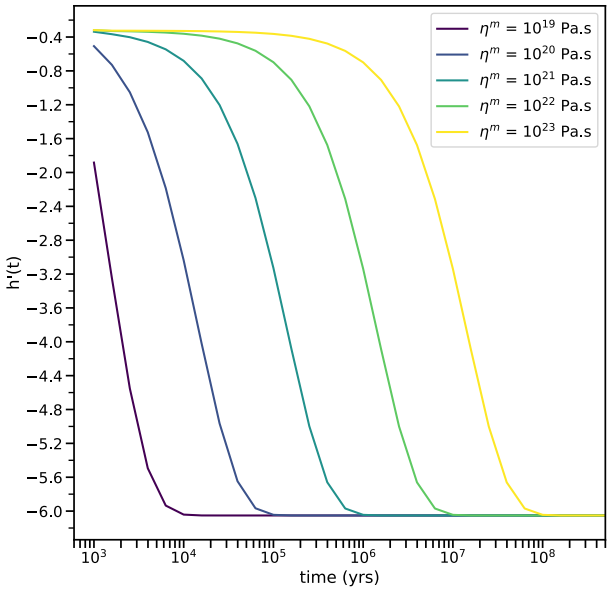

Figure S6. Degree-8 load Love number h' as a function of time for different mantle (η^m) viscosities. The elastic thickness of the lithosphere is set to 330 km, and its rigidity to 40 GPa. Following Phillips et al. (2008), we set the crustal thickness to 35 km, the mantle and core density to respectively 3500 and 6600 kg m^{-3}, and the core radius to 1700 km. A reasonable range for the present-day viscosity of the mantle is 10^{20} to 10^{22} Pa s (Plesa et al., 2018).